Supplementary material for: Distributed Wavefront Shaping in Near-Field sub-THz Wireless Networks

Atsutse Kludze[1], Duschia Bodet[2], Josep Miquel Jornet[2], and Yasaman Ghasempour[1*]

[1] Department of Electrical and Computer Engineering, Princeton University, 41 Olden St., Princeton NJ 08544, USA

[2] Department of Electrical and Computer Engineering, Institute for the Wireless Internet of Things, Northeastern University, Boston, MA, USA

Table of Contents

SUPPLEMENTARY NOTE I: DETAILING EM SIMULATIONS 2

SUPPLEMENTARY NOTE II: EXPERIMENTAL SETUP 4

SUPPLEMENTARY NOTE III: FAR-FIELD LINK BUDGET CALCULATIONS 7

SUPPLEMENTARY NOTE IV: NEAR FIELD POWER MEASUREMENT AND ELECTRIC FIELD MODEL DERIVATION 9

SUPPLEMENTARY NOTE V: SIMPLIFICATION OF NEAR FIELD RECEIVED POWER CALCULATION 11

SUPPLEMENTARY NOTE VI: EXAMPLE SPATIAL REPRESENTATION OF BEAMTYPE PHASE PROFILES 14

SUPPLEMENTARY NOTE VII: PHASE PROFILES FOR FOCUSED BEAM AND FAR-FIELD GAUSSIAN BEAM FOR SINGLE AND DISTRIBUTED ARRAY 16

SUPPLEMENTARY NOTE VIII. ENFR FOR BESSEL BEAMS AND AIRY BEAMS 18

SUPPLEMENTARY NOTE IX. DISTRIBUTED WAVEFRONT SHAPING BEYOND TWO APERTURES 23

SUPPLEMENTARY NOTE X. IMPACT OF ARRAY SEPARATION 25

REFERENCES 26

Supplementary Note I: Detailing EM Simulations

In this note, we provided detailed information about our EM simulations and power calculations. We used the EM simulator Altair FEKO to simulate near-field beams at the sub-THz frequencies. We create an array of ideal dipole sources tuned to specific amplitude and phase values for the desired electric field distribution, $E_o(x, y)$, across the array. This allows us to simulate the radiation behavior of any beam type, $E(x, y, z|E_o)$, without having to account for any non-idealities from each radiating element (as opposed to a physical element) that would distort its performance. Moreover, within the simulation, we can arrange the diploes in any arbitrary geometry pattern and adjust its element spacing as needed, as shown in Figure S1. Figure S2 illustrates the resulting E-field pattern of several near-field beamtypes and far-field Gaussian beams simulated in Altair FEKO.

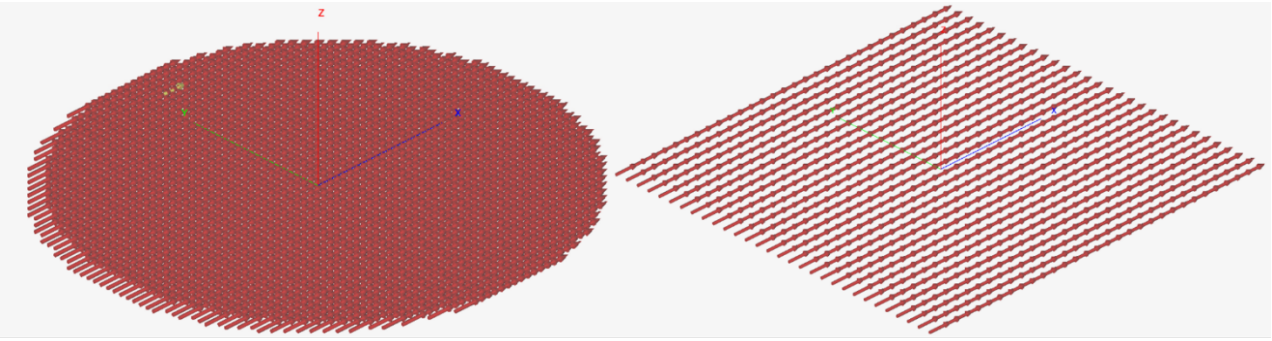

Figure S1 - Calculations of Numerical Results using FEKO Electromagnetic Simulation: An example configuration of an ideal phase array configured as a (a) uniform circular array and (b) a uniform rectangular array. The arrays are constructed using ideal electric dipole sources that can be set to any desired phase and amplitude value. Additionally, the arrays can be constructed using any desired element

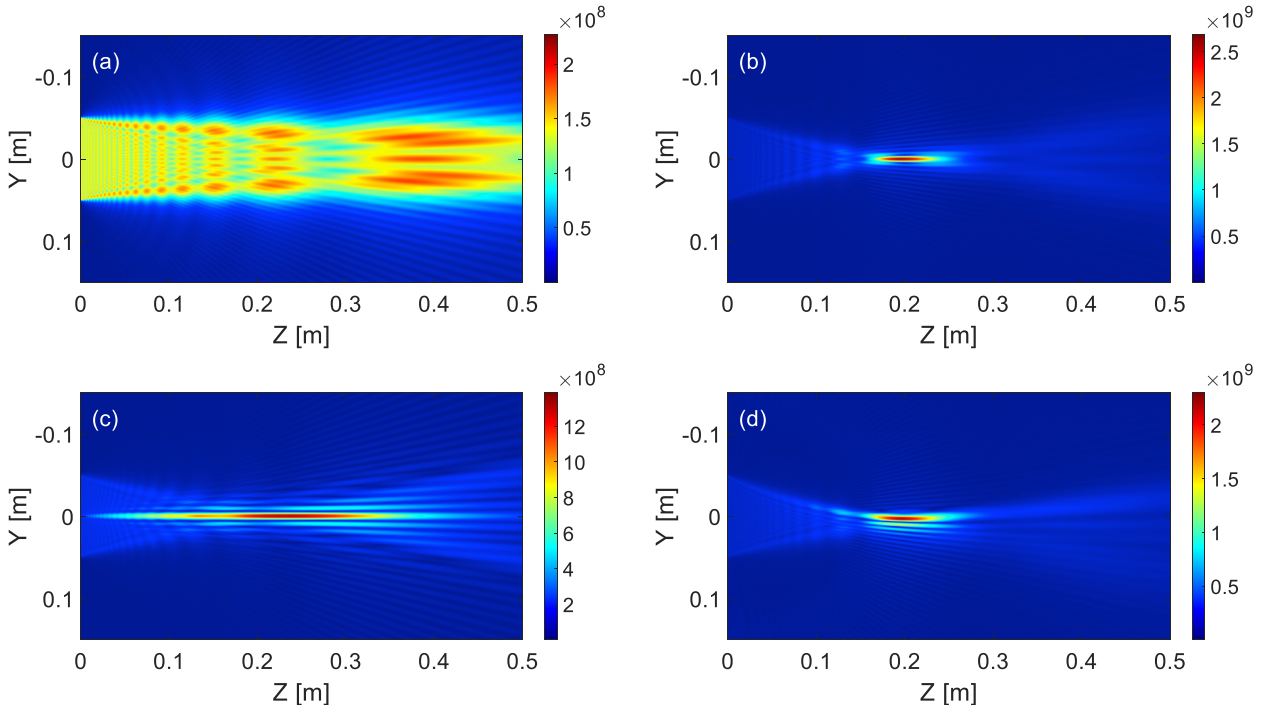

Figure. S2. Beamtype Simulations Generated in FEKO Altair. (a) Simulated Far-Field Gaussian Beam (b) Simulated Focused Beam (c) Simulated Bessel Beam (d) Simulated Airy Beam.

After simulation of the electric field profile across space, we calculate the power that transverses over the entire receiver area, A_{RX}:

$$P_{rx} = \iint |E(x', y', z'|E_o)|^2 \, dA_{rx} \quad (S1)$$

This represents the maximum obtainable power at the RX, i.e., when a received matched filter is adopted. This form of power calculation allows us to compare different beamtypes in a fair manner and independent of the receiver beamforming.

Supplementary Note II: Experimental Setup

Experimental setup. As briefly discussed in the Methods section of the supplemental, we conduct over-the-air experiments in the D-band (110 GHz-170 GHz). We performed these experiments using two separate setups – one used for small-scale and precise measurements and a second for larger-scale experimentation. For our small-scale experiment, we use the Keysight 306 PSG Analog Signal Generator (E8257D) as the local oscillator (LO) for up-conversion and down-conversion. An Agilent N5182A signal generator supplies the intermediate frequency (IF) signals. On the transmit side, the LO is fed into a 4× up-convertor from VDI (WR6.5CCU-M4) rated for the D-band. The transmitter is then placed near the metasurface for illumination. After up-conversion, the signal is transmitted through a horn antenna and a broadband amplifier (VDI WR6.5 AMP). To account for the transmitter emitting spherical wavefronts, where planar wavefronts are ideal, phase correction is applied to the phase distribution design of the metasurfaces. On the receiver side, we use the corresponding down-converter (WR6.6CCD-M4). Our receiver is placed on a motorized 3D translation stage for high-precision alignment and movement. The received signal is then fed into a Keysight Real-Time Oscilloscope (UXR0254B) for digitalization and further processing. For heatmap measurements, we measured the radiation

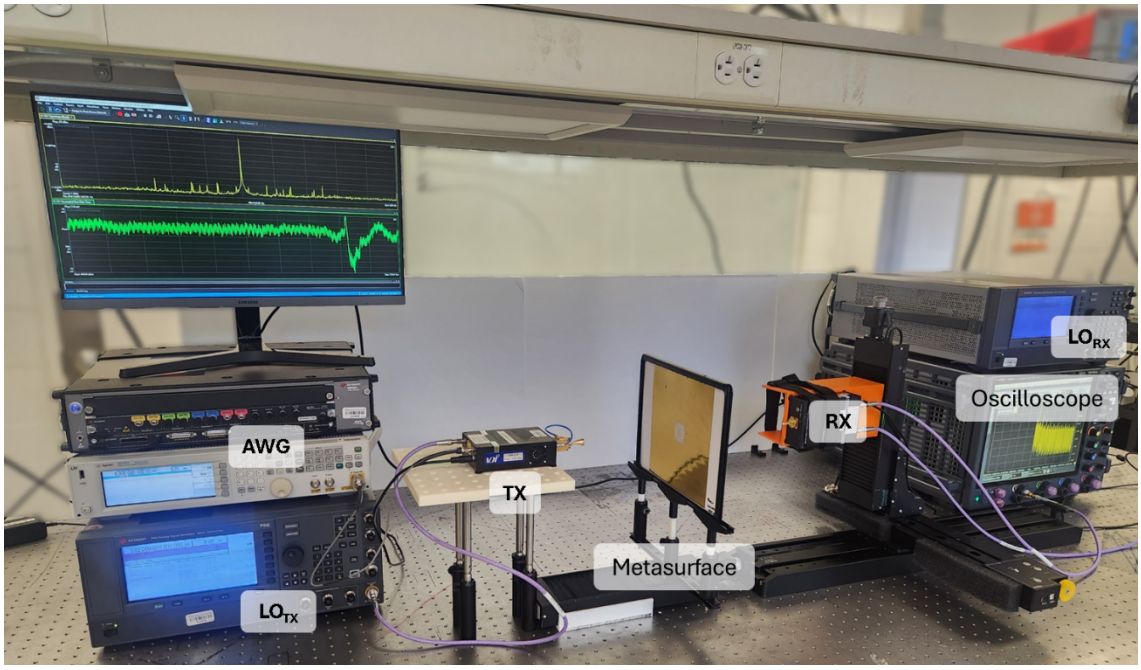

Figure S3 – Our scale model sub-THz setup for ENFR measurements

pattern by measuring the received power at each spatial location. An illustration of this setup is shown in Fig. S3.

For long-range verification of the ENFR we used custom-made, broadband D-band up-converters from Virginia Diodes (VDI). In this case, the local oscillator (LO) and IF signals are supplied to the VDI up-converter by two Keysight Performance Signal Generators (PSG E8257). For the transmitting antenna, we use Anteral LHA-HG-WR06, which contains a horn antenna and collimating lens in a compact structure. Thus, in the case of these experiments, the metasurface is placed directly in front of the lens and held in place by a 3D-printed cap. For the data transmission, the same configuration is used on the transmitter side, except that the LO signals are supplied by Berkeley Nucleonics Microwave Signal Generator 855B RF, and the IF signals are designed digitally in MATLAB, before being converted to analog and passed to the VDI up-converters using a Keysight Arbitrary Waveform Generator (AWG M8196A). At the receiver side, a VDI down-converter is used with a pyramidal horn antenna (Eravant SAR-1532-06-S2). The LO for down-conversion is supplied by a Keysight PSG, and the IF received signal is digitized and saved by a Keysight Digital Storage Oscilloscope (DSOZ632A). The digitized signal is then loaded into MATLAB for demodulation, equalization, and detection. An illustration of this setup can be found in the main manuscript in Figure 2 and Figure 6 of the main text.

Meatasurface Fabrication. To imitate the phased arrays that would be used in future sub-THz networks, we used passive metasurfaces in our over-the-air experiments where each unit cell is comprised of a C-shaped split-ring resonator. By changing the geometry of such resonators specifically, the radius, opening angle, and ring width, the phase of the cross-polarized transmission signal can be fine-tuned across a wide frequency range[1]. Thus, by creating an array of their resonators with each geometry corresponding to a cross-polarized phase shift, we create any desired beamtype pattern. We conduct a parameter sweep on resonator geometries in CST Studio Suite to generate a look-up table for phase modulation. The optimal metasurface array geometries can be quickly mapped from desired phase profiles. Our parameters were swept across a range such that their geometries never exceeded a $\frac{\lambda^2}{4}\left(\frac{\lambda}{2}\ \mathrm{x}\frac{\lambda}{2}\right)$ unit cell square area. Hence three different look-up tables were generated to create $\frac{\lambda}{2}$ unit cell resonators at 125 GHz, 145 GHz, and 165 GHz. We report an average phase error of $0.56°$ and an amplitude variance of

2.5517% across the full 360° phase modulation range. Once the metasurface geometry is determined, it is fabricated on US-letter-sized paper with the hot stamping technique[2]. First, a laser printer is used to print out the designed C-shaped resonator patterns. Then, we run the printed pattern together with aluminum foil through a standard office laminator. Under high temperatures, the aluminum powder on the foil adheres to the printed toner pattern to generate resonating metasurfaces.

Supplementary Note III: Far-Field Link Budget Calculations

Typically, link budget calculations are performed in the far-field, that is when electromagnetic propagation has reached a distance farther than the Fraunhofer distance. At this distance, the radiation pattern can be accurately modeled with several simplifications and assumptions. One of these simplifications is that we can perform link budget calculations using the Friss transmission equation.

If we assume that an array is given an initial power of $P_t(W)$ with a known Directivity gain of G_t, then the power density can be modeled as the total power over the surface area of a sphere with radius d:

$$p = \frac{P_t}{4\pi d^2} G_t \ (S2)$$

Given the known transmitted power density, the received power can be written as the transmitted power density integrated over the area that the receiver can capture the radiation:

$$P_r = \iint p \ dA_{RX} \ (S3)$$

Given that (1) the power density function at a fixed distance is a constant and (2) we can represent the area of the receiver's reception as its effective aperture area, Aperture area, A_{eff}, P_r simplifies to:

$$P_r = \ p \cdot A_{eff} = \frac{P_t}{4\pi d^2} G_t \ \cdot A_{eff} \ (S4)$$

Further, in most scenarios, the effective aperture of an antenna can be directly mapped to its directivity,

$$A_{eff} = \frac{\lambda^2}{4\pi} G_r \ (S5)$$

Thus, the equation can be rewritten as:

$$P_r = P_t \left(\frac{\lambda}{4\pi d}\right)^2 G_t G_r \ (S6)$$

Finally, in wireless channels that include other effects, such as obstruction or multi-path, we modified the equation to account for this by adding an α factor:

$$P_r = \alpha \cdot P_t \left(\frac{\lambda}{4\pi d}\right)^2 G_t G_r \ (S7)$$

While this equation can accurately model the received power for link-budget calculations, it fails to capture the distance and location-dependent radiation pattern in the near-field regime. Thus, accurate calculations require careful consideration of the transmitter and receiver's antenna properties, its location in space, and most importantly, its beamtype. Such calculations become even more complex in the presence of environmental factors (such as blockage) that alter the natural radiating behavior of the electromagnetic signal.

Supplementary Note IV: Near Field Power Measurement and Electric Field Model Derivation

Recall that the E-field profile from an aperture at any distance z can be modeled based on Eq.1 of the main text:

$$E(x,y,z) = F_k^{-1}\left[E_o\left(k_x,k_y\right)H\left(k_x,k_y,z\right)\right] \quad (1)$$

Such modeling is based on the Fourier optics concept of "angular spectrum of plane waves" where the resulting wavefront can be represented by a superposition of plane waves that propagate in different directions represented by wave-vector components $k_x \; and \; k_y$. Here, we only consider forward propagation ($z>0$) and that array is placed along the x-y plane. Thus, k_x and k_y can be written as $k_x = \left\|\frac{1}{\lambda}\right\| \sin\theta_{el} \cos\theta_{az}$ and $k_y = \left\|\frac{1}{\lambda}\right\| \sin\theta_{el} \sin\theta_{az}$. $k_x \; and \; k_y$ are refer to as the spatial frequencies as they represent the repeated pattern within the spatial domain. This is analogous to the time-based Fourier transformation where a time-domain signal is composed of a superposition of sinusoids of different frequencies. $H\left(k_x,k_y,z\right)$ represents the spatial transfer function of the propagation medium. If we assume a linear, isotropic, homogenous, and non-dispersive medium $H\left(k_x,k_y,z\right)$ becomes Weyl's, identity, written as $e^{i2\pi z\sqrt{\frac{1}{\lambda^2}-k_x^2-k_y^2}}$. In our formulation, we assume the medium is free-space air (corresponding to a n=1). If each sub-array is considered to be a portion of a larger virtual array, $E_o(x,y)$ can be written as:

$$E_o(x,y) = \sum_{n=1}^{N} \alpha_n(x,y) \exp j\phi_n(x,y) \quad (S8)$$

where $a_n(x,y)$ is the area where the transmitter(s) is active and $\emptyset_n(x,y)$ is the phase distribution for the desired beamtype of each transmitter. Thus, by applying the Fourier convolution property and the spatial shifting property, the spatial representation of Eq. S8 becomes:

$$E_o(k_x,k_y) = \sum_{n=1}^{N} e^{ik_x x_n} e^{ik_y y_n} \mathrm{A}_{tx.n}\left(k_x,k_y\right) * \Phi_{tx,n}\left(k_x,k_y\right) \quad (S9)$$

where $\mathrm{A}_{tx.n}(k_x, k_y) * \Phi_{tx,n}(k_x, k_y)$ is the convolution product of the input field's spatial coverage in the frequency domain (or in other words, the input field's amplitude Fourier transformation) and the input field's phase Fourier transformation. From this, we can represent the radiation of apertures as a spatial Fourier convolution. This holds for any arbitrary wavefront or the number of arrays.

Please Note that a single array is considered, Eq. S9 simplifies to

$$E_o(k_x, k_y) = e^{ik_x x_o} e^{ik_y y_o} \mathrm{A}_{tx}(k_x, k_y) * \Phi_{tx}(k_x, k_y) \ (S10)$$

Therefore, when measuring the received power, we insert Eq.S10 into Eq.3 to arrive at Eq.4 of the main text

$$P_{rx} = \iint \left\| F_k^{-1} \left[\left(e^{ik_x x_o} e^{ik_y y_o} A_{tx}(k_x, k_y) * \Phi_{tx}(k_x, k_y) \right) e^{i2\pi z \sqrt{\frac{1}{\lambda^2} - k_x^2 - k_y^2}} \right] \right\|^2 dA_{rx} \ (S11)$$

Supplementary Note V: Simplification of Near Field Received Power Calculation

As mentioned in the main text, Eq. S10 has no closed-form equation for all geometries. To illustrate this, we will for example sake that each of the arrays holds a rectangular geometry. Thus, $a_n(x, y)$ becomes

$$a_n(x',y') = \prod(\frac{x}{L_{n,x}} + x_n, \frac{y}{L_{n,y}} + y_n) \text{ (S12)}$$

Where its spatial representation equates to

$$A_{n,k}(k_x, k_y) \ = \ L_{n,x}\, L_{n,y}\, e^{ik_x x_n} e^{ik_y y_n} sinc(\frac{k_x L_{n,x}}{2})\ sinc(\frac{k_y L_{n,y}}{2}) \text{ (S13)}$$

If we assume a square array, $L_{n,x}$= $L_{n,x}$ = L

$$A_{n,k}(k_x, k_y) = L^2 e^{ik_x x_n} e^{ik_y y_n} sinc(\frac{k_x L}{2})\ sinc(\frac{k_y L}{2}) \text{ (S14)}$$

We can represent all propagating signals from square apertures regardless of their configuration as

$$E(x, y, z) =$$

$$F_k^{-1}\left[\left(\sum_{n=1}^{N} = L^2 e^{ik_x x_o} e^{ik_y y_o} e^{ik_y y_o} sinc(\frac{k_x L}{2})\ sinc(\frac{k_y L}{2})\ *\emptyset_{n,k}(k_x, k_y)\right) e^{i2\pi z\sqrt{\frac{1}{\lambda^2} - k_x^2 - k_y^2}}\right] \text{ (S15)}$$

Additionally, we can then calculate the maximum receiver power using Eq.3 in the main text:

$$P_{rx}$$

$$= \int \left\| F_k^{-1}\left[\left(\sum_{n=1}^{N} L^2 e^{ik_x x_n} e^{ik_y y_n} sinc(\frac{k_x L}{2})\ sinc(\frac{k_y L}{2})\ *\emptyset_{n,k}(k_x, k_y)\right) e^{ikz\sqrt{1 - k_x^2 - k_y^2}}\right]\right\|^2 dA_{rx} \text{ (S16)}$$

This formulation has no closed-form equation but can be calculated via the FFT algorithm. Simplification of Eq. S10 can only be achieved if: (1) the transmitter is infinitely large (a non-physical result) or (2) the resulting convolution in Eq. (S9) has an analytical solution. First, we will consider scenario (1).

We will assume a single aperture (N=1) centered at the origin ($\langle x_1, y_1 \rangle = \langle 0,0 \rangle$) for simplification.

If the transmitting aperture is infinitely large, then $a_1(x, y) = 1$. The Electric field profile at the transmitter can be written as

$$E_o(x, y) = \exp j\phi_n(x, y) \ (S16)$$

In such a scenario, the Fourier representation of the array, $A_{1,k}(k_x, k_y)$, becomes a delta function:

$$A_{1,k}(k_x, k_y) = \delta(k_x, k_y) = \begin{cases} 1 & if\ k_x = k_y = 0 \\ 0 & otherwise \end{cases} (S17)$$

Thus Eq. 1 in the main text becomes

$$E(x, y, z) = F_k^{-1}\left[\left(\delta(k_x, k_y) * \Phi_{tx}(k_x, k_y)\right) e^{i2\pi z\sqrt{\frac{1}{\lambda^2}-k_x^2-k_y^2}}\right] (S18)$$

Next, we can use the delta-function convolution property where $\delta(x) * f(x) = f(x)$ to further simplify Eq.S18 to

$$E(x, y, z) = F_k^{-1}\left[\Phi_{tx}(k_x, k_y) e^{i2\pi z\sqrt{\frac{1}{\lambda^2}-k_x^2-k_y^2}}\right] (S19)$$

Therefore, in the case of an infinite-sized aperture, the electric field profile can be modeled based on the product of the phase profile spatial representation and the transfer function of the corresponding medium. Finally, relating this to Eq. 3 in the main text:

$$P_{rx} = \iint |E(x', y', z'|E_o)|^2 \, dA_{rx}$$

$$= \int \left\| F_k^{-1}\left[\Phi_{tx}(k_x, k_y) e^{i2\pi z\sqrt{\frac{1}{\lambda^2}-k_x^2-k_y^2}}\right]\right\|^2 dA_{rx} \ (S20)$$

Next, we rederive Eq. S10 based on scenario (2). Once again, we assume a single aperture centered at the origin. Here, we assume $a_1(x, y)$ has a geometry follows the equation:

$$a_1(x, y) = sinc(\tfrac{x}{L_x}) sinc(\tfrac{y}{L_y}) \ (S21)$$

Where L_x and L_y are constants. Accordingly, $A_{1,k}(k_x, k_y)$ can be written as:

$$A_{1,k}(k_x, k_y) = \frac{L_x}{2\pi}\prod(L_x k_x)\frac{L_y}{2\pi}\prod(L_y k_y) \quad (S22)$$

Therefore, Eq. 1 in the main text is rewritten as

$$E(x,y,z) = F_k^{-1}\left[\left(\frac{L_x}{2\pi}\prod(L_x k_x)\frac{L_y}{2\pi}\prod(L_y k_y) * \Phi_{tx}(k_x, k_y)\right)e^{i2\pi z\sqrt{\frac{1}{\lambda^2}-k_x^2-k_y^2}}\right] \quad (S23)$$

We then use the convolution theorem $\prod(x) * f(x) = \int_{x-\frac{1}{2}}^{x+\frac{1}{2}} f(u)du$ To rewrite Eq. S23 as

$$E(x,y,z) = F_k^{-1}\left[\left(\frac{1}{4\pi^2}\int_{k_y-\frac{1}{2}}^{k_y+\frac{1}{2}}\int_{k_x-\frac{1}{2}}^{k_x+\frac{1}{2}}\Phi_{tx}(k_x, k_y)dk_{x'}dk_{y'}\right)e^{i2\pi z\sqrt{\frac{1}{\lambda^2}-k_x^2-k_y^2}}\right] \quad (S24)$$

In this configuration, the electric field profile can be described as the integrated results of the spatial phase profile multiple by the transfer function.

Please note that $\Phi_{tx}(k_x, k_y)$ also does not necessarily have an analytical expression for all possible phase profiles. We discuss this in Supplementary Note VI. Thus, even if the exact array geometry is analytically defined, it does not guarantee a closed expression. Further, in both derivations, we assume a single array with no spatial shift to reduce the equation's complexity. Thus, in general, Eq.4 of the main text cannot be solved without numerical methods.

Supplementary Note VI: Example Spatial Representation of Beamtype Phase Profiles

From Eq.4 of the main text, $\exp j\phi_n(x,y)$ represents the chosen phase distribution of the array. Specifically, in this section, we consider a focused beam and far-field Gaussian (beamforming) as example beamtypes. Their corresponding phase distribution at the transmit array is:

$$\exp j\phi_n(x,y) = \begin{cases} e^{-ik(x'\cos[\theta_{el,n}]*\sin[\theta_{az,n}]+y'\sin[\theta_{el,n}])}, & if\ beamsteering \\ e^{-ik\sqrt{(x'-x_r)^2+(y'-y_r)^2+{z_r}^2}}, & if\ focused\ beam \end{cases} (S25)$$

In the case of beamforming, its spatial domain representation has a closed-form expression:

$$\emptyset_{n,\lambda}(x',y') = 2\pi\delta\left(k_x - k\cos\left[\theta_{el,n}\right]\sin\left[\theta_{az,n}\right]\right)\delta\left(k_y - k\sin\left[\theta_{el,n}\right]\right)\ if\ beamsteering\ (S27)$$

A focused beam, however, does not, limiting accurate calculations to only numerical results. However, it can be closely approximated via Taylor expansion.

For example, sake, $x_r = y_r = 0$ and x' = x, $y' = y$

$$e^{-ik\sqrt{(x'-x_r)^2+(y'-y_r)^2+{z_r}^2}} = e^{-ik\sqrt{x^2+y^2+{z_r}^2}}\ (S28)$$

We can rewrite the exponent terms

$$\sqrt{x^2+y^2+{z_r}^2} = z_r\sqrt{1+\frac{x^2+y^2}{{z_r}^2}}\ (S29)$$

We can then approximate Eq. S25 in the form of Taylor Series of the first two terms

$$z_r\sqrt{1+\frac{x^2+y^2}{{z_r}^2}} \approx z_r + \frac{x^2+y^2}{2z_r} = f + \frac{x^2+y^2}{2f}\ (S30)$$

where f represents the focal distance. The first term can be omitted because it represents a constant phase shift across the aperture and does not affect the radiation behavior. Thus, the focused beam spatial Fourier representation can be approximated as:

$$F_k\left\{e^{-ik\sqrt{x^2+y^2+z_r{}^2}}\right\} \sim F_k\left\{e^{-ik\frac{x^2+y^2}{2f}}\right\} = \frac{1}{\sqrt{-\frac{k^2}{f^2}}} e^{\frac{\frac{k_x{}^2+k_y{}^2}{2}}{\sqrt{-\frac{k^2}{f^2}}}} = -i\beta e^{\frac{-i\beta(k_x{}^2+k_y{}^2)}{2}} \quad (S31)$$

Where $\beta = \frac{1}{\sqrt{\frac{k^2}{f^2}}} = \sqrt{\frac{f^2}{k^2}} = \sqrt{\frac{(\lambda f)^2}{4\pi^2}}$. We emphasize that the focused beam phase distribution in the spatial Fourier domain can be approximated in 3D space following Taylor expansions, where $x_r \neq y_r \neq 0$:

$$e^{-ik\sqrt{(x-x_r)^2+(y-y_r)^2+z_r{}^2}} \sim \sqrt{x_r{}^2+y_r{}^2+z_r{}^2} - \frac{y_r y}{\sqrt{x_r{}^2+y_r{}^2+z_r{}^2}} + \frac{y^2(x_r{}^2+z_r{}^2)}{2(x_r{}^2+y_r{}^2+z_r{}^2)^{\frac{3}{2}}} -$$
$$\frac{x_r x}{\sqrt{x_r{}^2+y_r{}^2+z_r{}^2}} - \frac{x_r y_r xy}{(x_r{}^2+y_r{}^2+z_r{}^2)^{\frac{3}{2}}} + \frac{x_r(x_r{}^2-2y_r{}^2+z_r{}^2)xy^2}{2(x_r{}^2+y_r{}^2+z_r{}^2)^{\frac{5}{2}}} + \frac{(y_r{}^2+z_r{}^2)x^2}{2(x_r{}^2+y_r{}^2+z_r{}^2)^{\frac{3}{2}}} +$$
$$\frac{y_r(-2x_r{}^2+y_r{}^2+z_r{}^2)yx^2}{2(x_r{}^2+y_r{}^2+z_r{}^2)^{\frac{5}{2}}} + \frac{(2x_r{}^4+y_r{}^4+y_r{}^2z_r{}^2-z_r{}^4+x_r{}^2(-11y^2+z^2))x^2y^2}{4(x_r{}^2+y_r{}^2+z_r{}^2)^{\frac{7}{2}}} \quad (S32)$$

Nonetheless, a closed form expression would require emission for several of the higher-order terms, meaning that such derivation would be only accurate for specific user locations.

We emphasize that an analytical expression for all phase distributions cannot be derived, as seen in the case of a focused beam, reaffirming that Eq. 4 of the main text requires numerical analysis.

Supplementary Note VII: Phase Profiles for Focused Beam and Far-field Gaussian Beam for Single and Distributed Array

A focused beam is the near-field equivalent of beamforming which focuses power on a specific point in space (as opposed to focusing on a specific direction). The phase distribution to generate this wavefront on a transmitting array needs to be configured such that the optical distance across all points of the array at the designated focal point is identical:

$$\emptyset(x, y) = -k\sqrt{(x - x_r)^2 + (y - y_r)^2 + {z_r}^2} \; (S33)$$

Where k is the free space wave number, and $\langle x_r, y_r, z_r \rangle$ is the focal point, the location of power concentration. Please note as the focal distance approaches infinity, Eq. S33 becomes indistinguishable from traditional beamforming (Far-Field Gaussian). Its phase profile replicates the phase distribution of a homogeneous optical lens. An example of its phase distribution is shown in Figure S4.

When the beamtype is configured instead for far-field Gaussian, the only parameter that can be tuned is the steering angle. From this, the phase distribution is configured to a linear ramp following the equation.

$$\emptyset(x, y) = k(x \cos[\theta_{el}] * \sin[\theta_{az}] + y \sin[\theta_{el}]) \; (S34)$$

Where θ_{el} and θ_{az} is the designated elevation and azimuth steering angle respectively. Its phase distribution is shown in Figure S5.

Please note that Eq.S33 and Eq.S34 apply for a single array. When distributed arrays are implemented a binary area coverage function is introduced. It represents that represents the placement of the array as a binary function $\alpha(x, y)$ where $\alpha(x, y) = 0$ at locations where the arrays are not active. If we divide $\alpha(x, y)$ into subarrays, $a_n(x, y)$, the phase distribution now becomes

$$\emptyset(x,y) = \sum a_n(x,y)\emptyset_n(x,y)\ (S35)$$

Because a focused beam's phase distribution is calculated based on the optimal optical distance at each location, Eq. S33 can be used for all arrays. However, for beamforming, the phase distribution needs to be calculated independently with the steering angles configured to steer at the receiver's location.

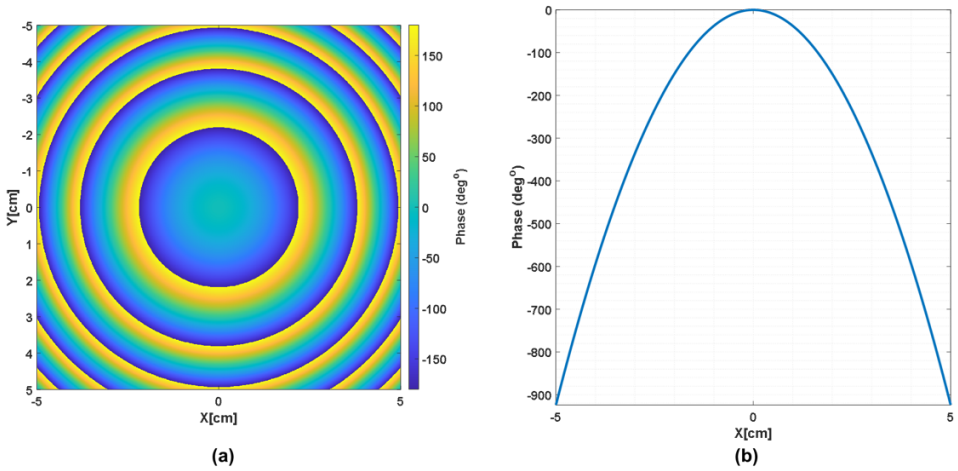

Figure S4 – Phase profile of a focused beam – a. Two-dimensional Phase Profile **b.** One-dimensional phase unwrapped profile.

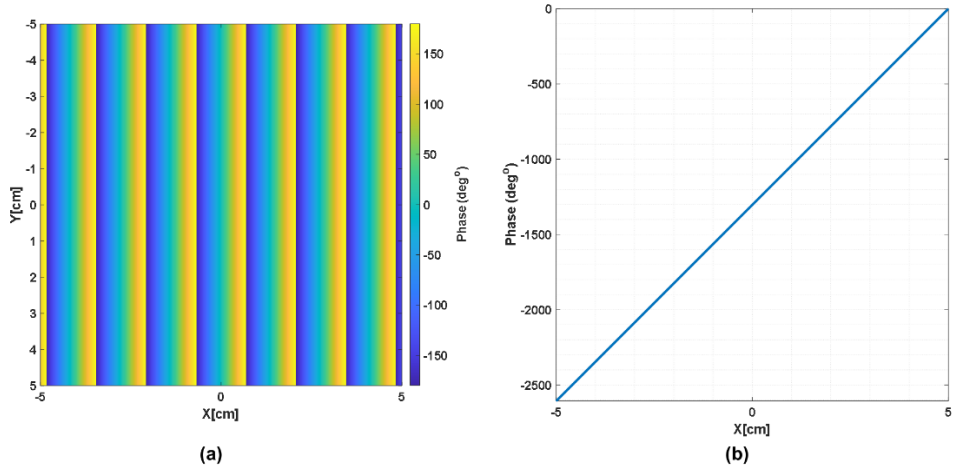

Figure S5 – Phase profile of a Steering Far-Field Gaussian Beam – a. Two-dimensional Phase Profile **b.** One-dimensional phase unwrapped profile.

Supplementary Note VIII. ENFR for Bessel Beams and Airy Beams

ENRF For Bessel Beam. In the main manuscript, we focused on developing a criteria of the ENFR for the focused beam beamtype. In the case of a focused beam, which as the name implies focuses power on a specific point in space, the ENFR should be characterized by how well power is consolidated at a certain location. However, if the same metric is applied for other wavefronts, such as a Bessel beam or any airy beam, then these beams would be unfairly deemed 'impractical'. However, we emphasize that the definition of ENFR is dependent on the beamtype given their very diverse characteristics.

First, we define the ENFR of Bessel beams. Bessel beams are designed to have non-diffraction radiation; that is, their intensity is independent of distance and does not cause any spreading losses. Due to this, instead of concentrating power in a specific location, Bessel beams focus along a specific line, which allows for relaxed localization information requirements. This makes Bessel beams better suited for mobile users or users with location uncertainty[3]. Additionally, due to their non-diffracting characteristics, Bessel beams are resilient to blockage; even if a portion of the wavefront is blocked, the remaining portion will be reconstructed after the obstruction (this property is often referred to as self-healing)[4]. Their wavefront can be described as having a set of plane waves traveling in an inward direction. The phase distribution on the transmit array required to generate this beam resembles an axicon where it has a radially symmetric phase gradient set by parameter α[5]:

$$\emptyset(x,y) = -k\sqrt{x^2 + y^2}sin\alpha \quad (S36)$$

An example phase distribution is provided in Figure S6. An ideal Bessel Beam is non-diffraction for all distances, but this requires an infinite size aperture. Since both conditions are infeasible in practice, the non-diffraction region is limited to the transmitter's dimension. The region of non-diffraction can be written as

$$Z_{max} = \frac{D}{2tan\alpha}(S37)$$

where D is the diagonal length of the array and Z_{max} is the maximum distance where the beam can be considered non-diffraction. In the case of Bessel beams, it is desired that their power gain (compared for far-field Gaussian Beam) across a set region is non-negligible. At first glance Eq.S37 implies that as long as $0^o < \alpha < 90^o$, it is possible to set a Z_{max} for any distance. While in principle true, in reality, the practical limit where noticeable gain is achieved (compared to far-field Gaussian beams) is much shorter. Thus, the ENFR for Bessel beams should be defined as **the maximum distance from the power gain across Z_{max} is greater than a 3dB threshold.** We present the heatmap of Bessel beams and their corresponding average power gain within the non-diffraction region in Figure S7 and Figure S8 respectively. In these simulations, we consider a 3.5cm x3.5xcm array (corresponding to D = 5cm) at a center frequency of 125 GHz. Once the Bessel beam is configured to a Z_{max} of 61cm (corresponding to $\alpha = 2.3^o$) the average gain now reduces to below 3dB. Such distance is still lower than the desired Fraunhofer distance (1.0215m).

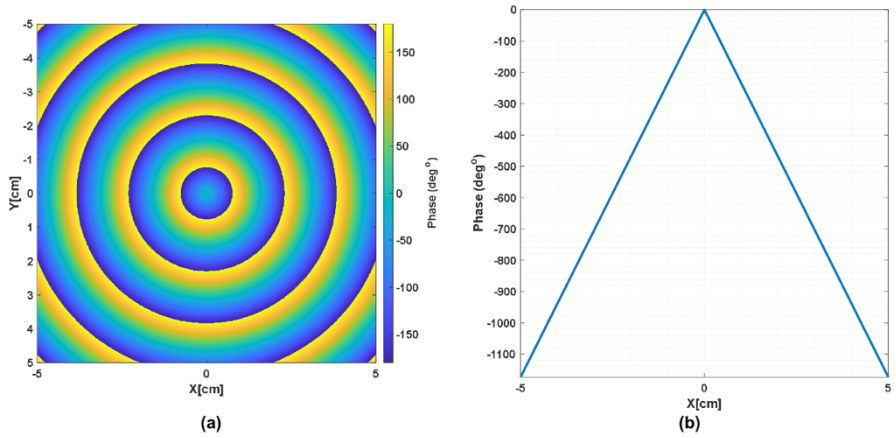

Figure S6 – Phase profile of a Bessel Beam – a. Two-dimensional Phase Profile **b.** One-dimensional phase unwrapped profile.

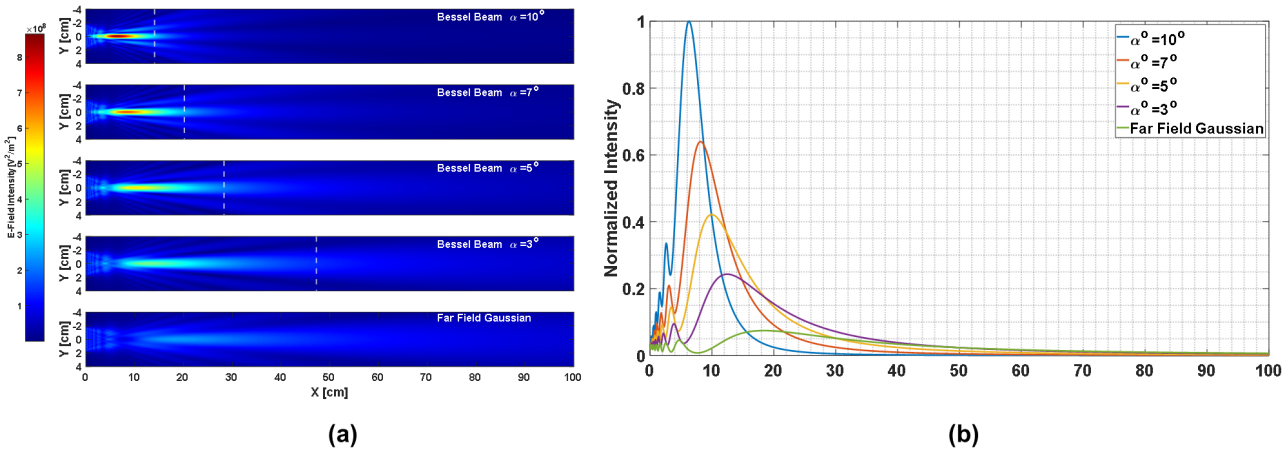

Figure S7 – Effective Near Field Range Simulation of Bessel Beam a. The simulated radiation behavior of a 3.5cm x3.5cm array configured to generate Bessel beams across different Z_{max} distances. Z_{max} is represented by the dash vertical lines **b.** The normalized intensity across the arrays' geometric center. As the desired Z_{max} increases, it is evident that the resulting intensity decays accordingly.

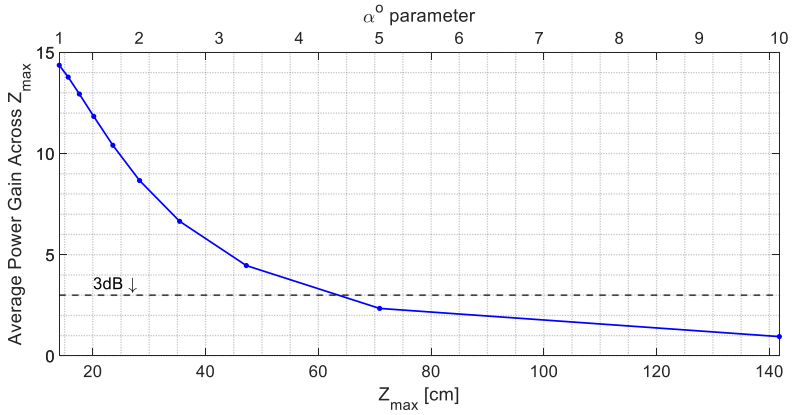

Figure S8 – Average power gain of Bessel over Gaussian as a function of Z_{max}

ENRF For Airy Beam. Next, we will focus on another type of particular non-spherical wave, the Airy beam, as it provides the most intriguing possibility for blockage avoidance. In the near field region, the Airy wavefront is both self-accelerating (its main lobe follows a curved trajectory in free space) and non-diffracting. Its 1D electric field profile can be modeled as:

$$E(x,z) = Ai\left(\frac{x}{x_o} - \frac{z^2}{4k^2{x_o}^4} + i\frac{\alpha z}{k{x_o}^2}\right) e^{i\frac{z}{2k{x_o}^2}\left(\frac{x}{x_o} - \frac{z^2}{6k^2{x_o}^4} + \alpha^2\right)} e^{\frac{\alpha}{x_o}\left(x - \frac{z^2}{2k^2{x_o}^3}\right)} \quad \text{(S38)}$$

where $Ai(\cdot)$ is the Airy function. The truncation parameter α represents the physical realization of Airy beams with finite aperture size (and therefore energy), x_o is a transverse scale parameter that determines the curvature beam. To generate this wavefront, the array must exhibit amplitude control (as opposed to phase for most other beamtypes). Therefore, the electric field at the transmitter must resemble the electric field distribution $E(x,0) = Ai\left(\frac{x}{x_o}\right)$, as shown in Figure S9. Under ideal infinite-power and infinite sized apertures, where $\alpha = 0$, the Airy Beam follows a propagating trajectory of $x(z) = \frac{z^2}{4k^2{x_o}^3}$. The parabolic trajectory can be tuned by varying parameter x_o. An example radiation pattern of an Airy Beam is shown in Figure S10. Nonetheless, Eq. S38 assumes that minimal diffraction occurs and that the aperture is orders of magnitude larger than the wavelength. While true in optics, it is not necessarily valid in the sub-THz regime. Additionally, self-acceleration and curving start at the transmit array, limiting the effectiveness of the curvature. Due to this, there is practical consideration in which where at a certain distance, the curvature enacted with the Airy Beam has a minimal effect. To illustrate we plot the curving trajectory of the Airy beams with various $x_o$confiugrations in Figure S11. These Airy beams were generated at a center frequency of 125GHz and the array size fixed to 10cm. As observed, as one wants to generate a curved path originating at a farther distance, the resulting curvature is reduced. This implies a finite range in which any meaningful curvature can be obtained for object avoidance. With consideration of Airy beams, the ENFR should be defined as **the maximum distance in which a desired curvature profile can be generated.**

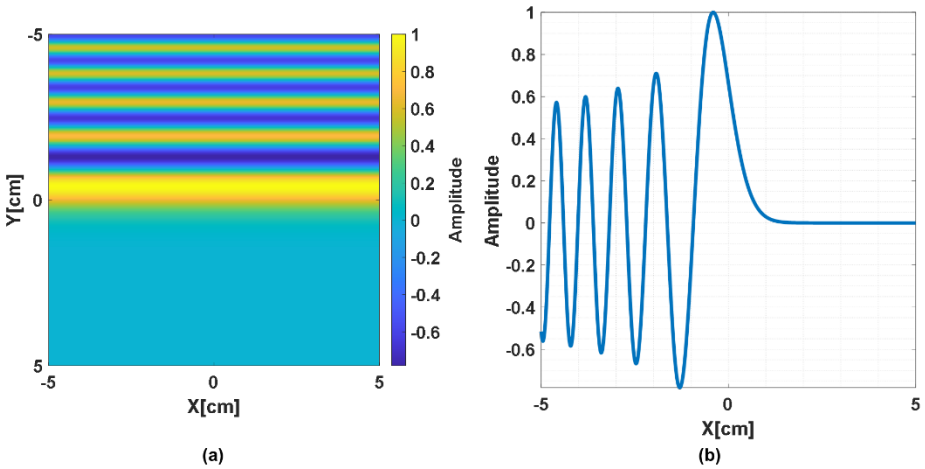

Figure S9 – Amplitude profile of an Airy Beam – a. Two-dimensional Amplitude Profile **b.** One-dimensional amplitude profile

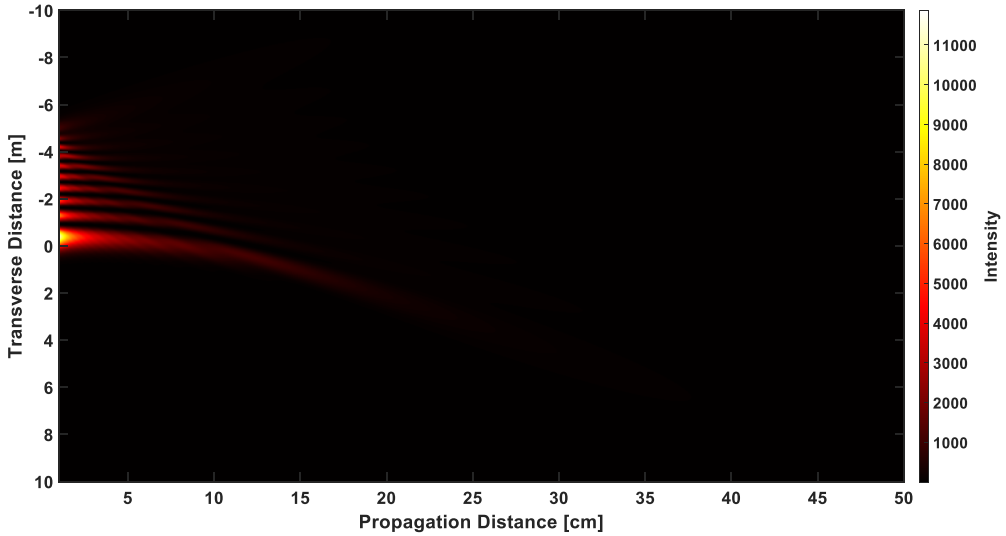

Figure S10 – Radiation Pattern of an Airy Beam, x_o= 4mm

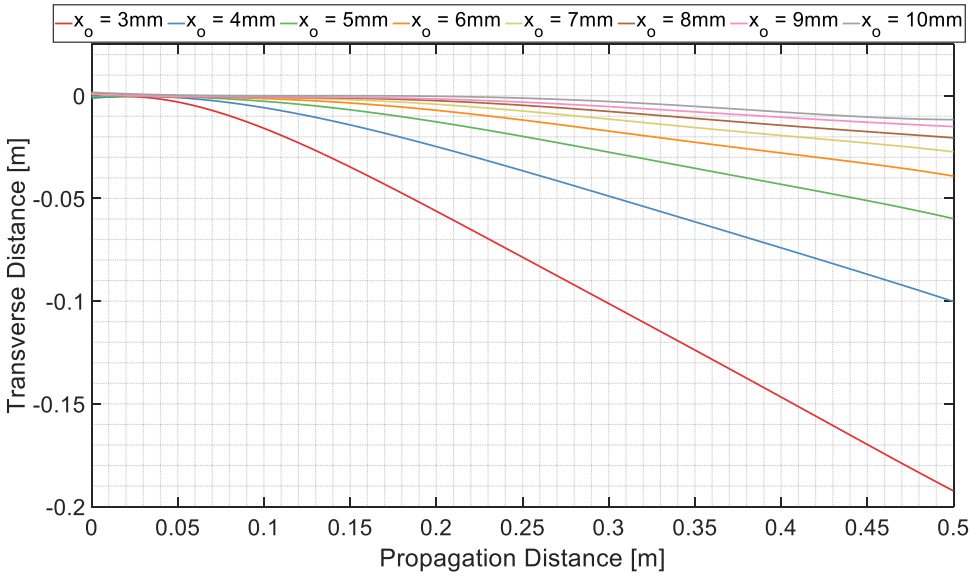

Figure S11 – ENFR Simulation of Airy Beam. Curving Trajectory Modeling of Air Beams with Finite Aperture Size

Supplementary Note IX. Distributed Wavefront Shaping Beyond Two Apertures

Although we focused on two arrays for distributed wavefront shaping in the main text, we note that such calculations hold for any arbitrary set of arrays. Particularly, Eq.6 makes no assumption on the number of arrays and the ENFR can be calculated accordingly. To illustrate this, we present simulation results considering 3 arrays working together to create a focused beam. A depiction of their placement is illustrated in Figure S12. Each array is 3.5cm x3.5cm with a separation of 4cm from each other. First, we plot its focusing gain at 125GHz across its radial map, as it was done in Figure 3 of the main text and is shown in Figure S13. Similar to the observations from two arrays, fluctuations from the focusing gain occur from the inconsistent superposition of the beamforming arrays. These fluctuations result in a more significant drop in beamforming power (increasing focusing gain) however from the higher coordination requirements. Nevertheless, we compare the $ENFR_{dst}$ (from Eq.7 of the main text) of the single array and its 2-array counterparts in Fig.S14. As observed, as the number of transmitting arrays increase, so can $ENFR_{dst}$ .We note however this is dependent on the array separation and location and is not a strictly true. Based on the configuration of 3-distributed array, the $ENFR_{dst}$ now extends to 99.45cm, which is 282% higher than the 2 arrays and 448% higher than a the single array. More importantly, the $ENFR_{dst}$ is now on a comparable distance as the Fraunhofer distance (1.0215m). Such results imply that increasing the number of distributed arrays can provide significant improvement to the $ENFR_{dst}$.

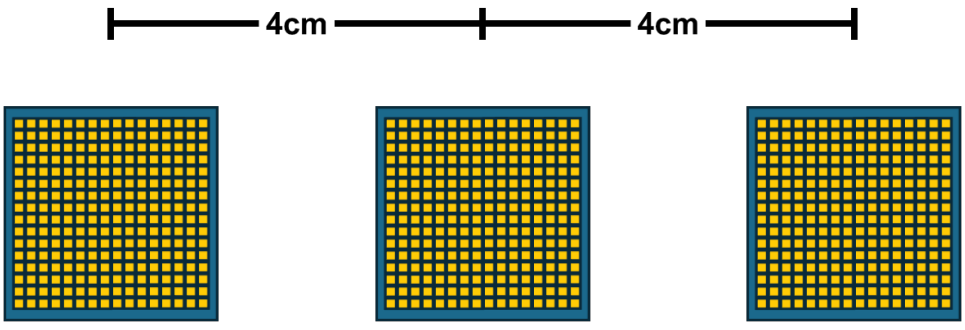

Figure S12 – Example Configuration of Distributed Wavefront Shaping with 3 arrays. Each arrays are placed equidistant with a separation of 4cm

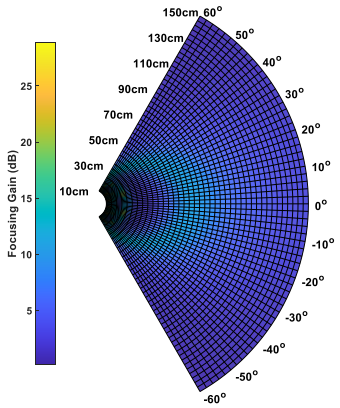

Figure S13 – Radial Map of the Focusing Gain for Distributed arrays. Similar to the two-array scenario, the focusing gain is not only a function of distance but also steering angle.

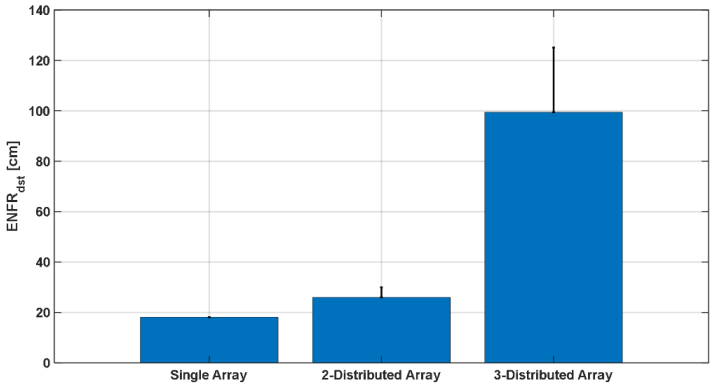

Figure S14 – Comparison of $ENFR_{dst}$ from different array configurations. As the number of apertures increases, the $ENFR_{dst}$ also increases accordingly. Such an increase is not linear and depends on several factors. The errorbar represents the maximum reported ENFR at a particular angle.

Supplementary Note X. Impact of Array Separation

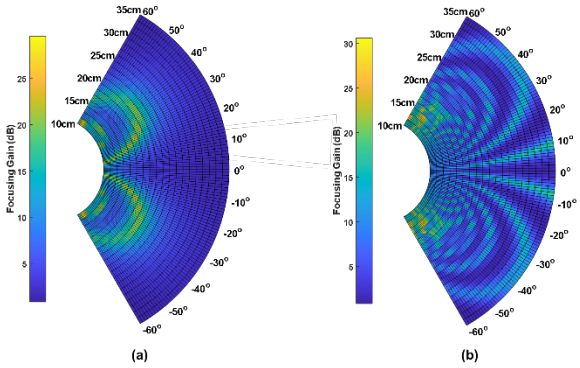

Figure S15 – Radial Map of Focusing Gain of Two Distributed Apertures – a. Array Separation:8cm **b.** Array Separation:16cm

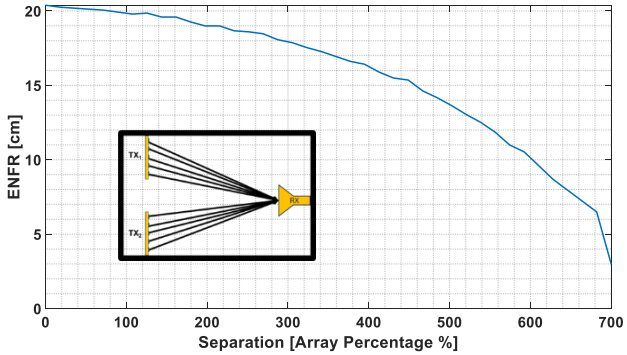

Figure S16 – ENFR Measurement of Distributed Arrays at Broadside

In the main text, we focused our analysis on a fixed separation of 8cm (measured from center to center). However, we emphasize that the separation of the arrays impacts the ENFR. To illustrate this, we plot the focusing gain of two different distributed array configurations; both utilize two 3.5cm x 3.5cm arrays at 125GHz but each setup has a separation of 8cm and 16cm respectively. A side-by-side comparison in Figure S15 reveals that increasing the separation increases the overall fluctuations over the radial maps. This mainly results from the fact that as the arrays becomes less co-located, their transmission ranges correlate less, and the constructive/destructive interference varies more. Nevertheless, these fluctuations result in focusing gains that are lower in magnitude. Thus, results imply that careful calibration between the arrays is even more crucial when a receiver is placed off-boresight. However, when a receiver is placed in the geometric center of two arrays (broadsight) where perfectly constructive interference is ensured for distributed beamforming, we see a clearer trend of the ENFR. In Figure S16, we plot the ENFR at broadside at different separations. We report the separation as a percentage of its subarray dimensions (3.5cm). Here, we see the ENFR degrading to half of its maximum range after a separation of 600% (21 cm). These results thus imply that as the separation between the arrays increases, its ENFR decreases.

References

1. Liu, L. *et al.* Broadband metasurfaces with simultaneous control of phase and amplitude. *Adv. Mater.* **26**, 5031–5036 (2014).
2. Guerboukha, H., Amarasinghe, Y., Shrestha, R., Pizzuto, A. & Mittleman, D. M. High-volume rapid prototyping technique for terahertz metallic metasurfaces. *Opt. Express* **29**, 13806–13814 (2021).
3. Petrov, V., Guerboukha, H., Mittleman, D. M. & Singh, A. Wavefront hopping: An enabler for reliable and secure near field terahertz communications in 6G and beyond. *IEEE Wirel. Commun.* **31**, 48–55 (2024).
4. Reddy, I. V. A. K. *et al.* Ultrabroadband terahertz-band communications with self-healing bessel beams. *Commun Eng* **2**, 1–9 (2023).
5. Singh, A., Reddy, I. V. A. K., Bodet, D. & Jornet, J. M. Bessel beams for 6G - A performance analysis. in *2022 56th Asilomar Conference on Signals, Systems, and Computers* 658–664 (IEEE, 2022).